This is the accepted version of:

Alina Samusenko, Davide Gandolfi, Georg Pucker, Tatevik Chalyan, Romain Guider, Mher Ghulinyan, and Lorenzo Pavesi, A SiON Microring **Resonator-Based Platform for Biosensing at 850 nm**, JOURNAL OF LIGHTWAVE TECHNOLOGY, Volume: 34, Issue: 3, Feb.1, 2016, pp. 969 – 977
DOI: 10.1109/JLT.2016.2516758

The final published version is available online at: https://ieeexplore.ieee.org/document/7384690

When citing, please refer to the published version.

A SiON microring resonator-based platform for biosensing at 850 nm

Alina Samusenko[1, 2], Davide Gandolfi[1], Georg Pucker[2], Tatevik Chalyan[1], Romain Guider[1], Mher Ghulinyan[2], and Lorenzo Pavesi[1]

***Abstract* — In this paper we report on the design, fabrication and characterization of a photonic circuit for biosensing applications. Silicon oxynitride with a bulk refractive index of 1.66 is the core-layer material. The photonic circuit is optimized for a wavelength of ~850 nm, which allows on-chip integration of the light source via cost effective vertical-cavity surface-emitting lasers and of the detector by using standard silicon photodetectors. Design as well as fabrication processes are explained in details. The best characteristics for the single optical components in the photonic circuit are: for single-mode channel waveguides with dimensions of 350 nm × 950 nm; propagation losses of 0.8 dB/cm; bending losses of 0.1 dB/90^0-bend (radius of curvature 100 μm); 49/51 splitting ratio for 3-dB power splitters (directional couplers); quality factors up to 1.3×10^5 for microring resonators. Volumetric sensing yields a bulk sensitivity of 80 nm/RIU and a limit of detection of 3×10^{-6} RIU. Therefore, SiON-based photonic circuits represent a reliable material platform for biosensing in the short-wave near infrared region.**

***Index Terms* — Biosensor, directional coupler, near infrared, photonic circuit, ring resonator, silicon oxynitride, waveguide.**

I. Introduction

In the last two decades new integrated optical sensor systems for laboratory use have been commercialized [1] by a number of companies like *Farfield, SRU Biosystems, Corning, Axela, Microvacuum* or *Genalyte.* These systems, which are essentially evanescent field sensors, have proved the superiority of optical methods in terms of sensitivity and automation. In addition, clinical diagnostics, environmental monitoring and food industry have a particular need for small, easy-to-use, portable and robust real-time diagnostic instruments. Ideally, in these so-called lab-on-a-chip (LOC) devices all functionalities – from sample preparation to signal delivery – are integrated on the same platform. Optical sensors offer a great potential for integration and fabrication using cheap and mature technologies. While the majority of optical biosensors are based on Surface Plasmon Resonance (SPR) techniques [2], there is also an evident trend towards the development of photonic sensors with a potential for on chip integration [1, 3].

In recent years, whispering-gallery mode (WGM) microring resonators are increasingly gaining attention as biological transducers due to their high spectral resolution, miniature size, ability to be densely arrayed and integrated into portable LOC instruments for multianalyte detection [4-8]. In particular, silicon-on-insulator (SOI) microring-based sensors have been demonstrated as highly sensitive and miniature detectors of biomolecules in various applications [9-11]. Some commercial apparatus have already been introduced to the market, e.g., the multiplexed assay platform Maverick™ by *Genalyte*, where an array of microring resonators is integrated on a single chip [12].

The SOI sensors operate at the telecommunication wavelengths around 1550 nm. For LOC biosensing devices the short-wave near infrared (SW-NIR) region between 700 nm and 900 nm represents an interesting alternative [13]. This is particularly true if the analyte is present in an aqueous system. In fact, the water absorption coefficient at these wavelengths is about 0.043 1/cm (0.19 dB/cm), which is three orders of magnitude lower than at 1550 nm [14]. Another motivation for investigating photonic circuits in the SW-NIR region comes from the fact that low-cost vertical-cavity surface-emitting lasers (VCSEL), emitting at around 850 nm, can be used as light sources [15] and silicon photodiodes as photodetectors [16]. Such integration of a light source, a detector and a sensor on the very same chip can permit the realization of tiny, robust and cheap optical biosensors, which do not require alignment of optical components and can give an important contribution towards the simplification of the development of compact LOC devices.

The passive optical circuits in the SW-NIR region can be realized either in Si_3N_4 or SiO_xN_y. Silicon oxynitride (SiON) has already been successfully employed as a CMOS-compatible material for the development of biosensing devices, such as Mach-Zehnder interferometers [17, 18], dual-slab waveguide interferometers [19] and waveguides for absorption-based sensors [20]. Recently we validated the use of SiON as a platform for microring-based biosensing [21-23], applied to the problem of detection of aflatoxin in milk. In this paper we explain reliable simulation methods for design and optimization of such photonic sensor and present a detailed analysis of the influence of fabrication uncertainties on the device performance. With respect to our preliminary work, we changed partially the circuit design and optimized the fabrication process (in particular, lithography and etching parameters) in order to improve the robustness of the device and its optical characteristics.

Generally, the detection with WGM resonators consists in the relationship of the resonance wavelength shift with the

[1] University of Trento, Nanoscience Laboratory, Department of Physics, Via Sommarive 14, Povo, Italy;
[2] Fondazione Bruno Kessler, Centre for Materials and Microsystems, Via Sommarive 18, Povo, Italy

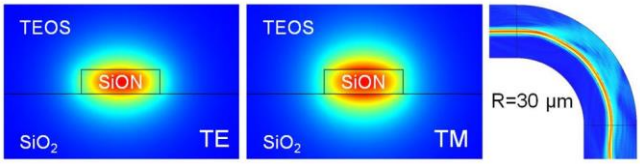

Fig. 1. Electric field profiles of TE and TM modes in the 300 nm × 1000 nm waveguide cross-section. On the right: top-view simulation of the bent waveguide, demonstrating the radiation in a sharp curve (λ=850 nm).

presence of analyte in the sample. The molecules of interest are recognized and trapped on the surface of the sensor, where they interact with the evanescent field of the propagating light. The sensor's sensitivity depends on the amount of evanescent field interacting with sensing solution. The circulating nature of light inside the ring favours the light-matter interaction since the analyte is probed multiple times. It has been demonstrated (see for example [24]) that bulk sensitivity of microring sensor can be enhanced by reducing the light confinement in the cavity, governed mainly by the control of the resonator thickness, on the cost of reduction of its quality factor (Q). On the other hand, high Q, meaning well-resolved spectral peaks, is desired for high sensing resolution.

Since the quality factor is primarily limited by optical losses, the important objectives are to minimize the intrinsic cavity losses and to provide efficient coupling of the light into the ring. Furthermore, in order to guarantee a multiplexed analysis, accurate splitting of input light in several sensors, fitted on a single chip, is necessary. In order to meet these requirements, we first developed individual components constituting the circuit, and consequently integrated them in a single device. The optical circuit is designed such to be integrated with VCSEL diode emitting at the wavelength (λ) of ~850 nm.

II. Design

A. Waveguide

The design of the channel waveguides, both straight and bent ones, was performed by Finite Element Method (FEM) simulations. First, the electric field profiles have been calculated and examined for a variety of dimensions with a mode solver in order to determine single-mode conditions for a 300 nm-high waveguide with SiON bulk refractive index of 1.66. The refractive index of the cladding is set to 1.46, which

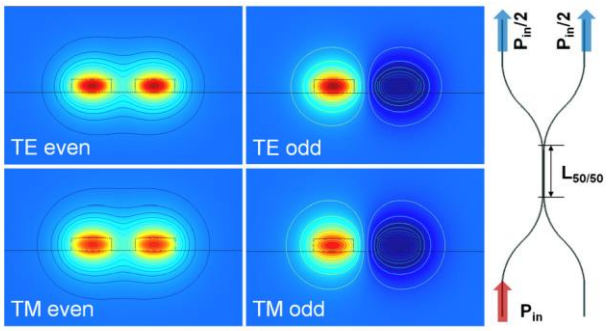

Fig. 2. Electric field profiles of even and odd TE/TM modes and scheme of the directional coupler for 50/50 power splitting.

Table I
Calculated 3dB-coupling length in μm

Waveguide width	900 nm		1000 nm	
Polarization	TE	TM	TE	TM
Covered with TEOS	50	42	64	52
Exposed to water	76	50	102	64

corresponds to the measured n of the silicon dioxides used in fabrication. According to the simulations, a waveguide with a width (W) smaller than 1.2 μm would assure single mode propagation at 850 nm for both polarizations. To ensure a more robust configuration, it is preferable to design narrower waveguides. However, for smaller widths the propagation losses of the waveguide increase significantly. For this reason we have chosen the widths of 900 nm and 1000 nm in the following design. Fig. 1 shows the electric filed profiles of the fundamental transverse electric (TE) and transverse magnetic (TM) modes of 1μm-wide waveguide with confinement factors of 59% (n_{eff}=1.513) and 46% (n_{eff}=1.502), respectively.

A mode, propagating in a bent channel waveguide, loses a part of energy mostly due to radiation and mode mismatch between the straight and the bent part of the waveguide. Traveling through a sharp curve, the mode field deforms and radiates out of the core largely. These losses are more evident for waveguides with low core-cladding refractive index contrast, therefore they are more relevant for a SiON waveguide surrounded with SiO_2, rather than for the waveguide immersed in water. Since bent waveguides are indispensable components of an integrated circuit, the bending losses have to be estimated to define the minimal allowable bending radius.

We performed FEM simulations of light propagation in a 90^0-curve with constant radius, converting a complex 3D model into a simpler 2D top-view problem as shown in Fig. 1. From the calculations, we found negligible radiation losses (less than 10^{-3} dB/90^0) for bends with radius higher than 100 μm, while a fast exponential increase of losses was observed for smaller radii. Indeed, they exceed the value of 1 dB/cm as soon as the bend radius is reduced to 75 μm. In order to confirm the theoretical analysis and to evaluate the contribution of surface-roughness-related scattering losses, we designed test structures with different bending radii (50, 75, 100 μm) for optical characterization.

B. Directional coupler

The multiplex detection requires the light to be directed equally to several sensing sites. Generally, optical power on the chip is distributed by either Y-branch splitters or 3-dB directional couplers. Since the lithographic system used for fabrication of our chips allows only for a minimum feature size of 380 nm, Y-branch splitters are not a convenient choice, as they require precise definition of the junction tip. On the contrary, the use of a 3-dB directional coupler is preferable since it allows relatively large separation between waveguides on the cost of the length of coupling region.

Besides, the directional coupler concept may be adopted for effective coupling of light into the racetrack-shaped ring resonator [25]. In the latter case, in the coupler design, we should consider water as a top cladding since the resonator has to be immersed in aqueous solution in order to be employed as a biosensor.

The design of the splitter was performed using the coupled mode theory, analyzing the transfer of power between two parallel identical waveguides. In this concept, the 50/50-coupling length can be calculated as [26]:

$$L_{50/50}[\mu m] = \frac{\lambda[\mu m]}{4(n_{eff.even} - n_{eff.odd})}, \quad (1)$$

where $n_{eff.even}$ and $n_{eff.odd}$ are the effective indices of symmetric (even) and antisymmetric (odd) eigenmodes, and λ is the operating wavelength. Fig. 2 shows the simulated field profiles of even and odd TE/TM modes of two parallel SiON waveguides with a separation of 600 nm between them, while Table 1 gives the results of the coupling length calculations for 900 nm and 1000 nm-wide waveguides covered with both TEOS-oxide (n=1.46) and water (n=1.33). It is clear that for smaller width, vertical (TM) polarization and lower core-cladding index contrast (SiON-TEOS) the optical modes are less confined in the core, and that there is a stronger evanescent field overlap between the waveguides. Accordingly, the power transfer occurs faster and a shorter coupling zone is required.

We also considered possible change of lateral waveguide geometry due to lithography errors and found that 10% width deviation would cause the change in coupling length of about 10%. In order to verify the calculations and obtain the optimal 3-dB splitting we designed directional couplers with various coupling lengths for both waveguide widths.

C. Microring resonator

Our microring resonators were designed considering the following requirements: (i) the dimensions of the sensor ring convenient also for functionalization with a microarray spotter (Biorad BioOdyssey™ Calligrapher™ MiniArrayer), which generally allows for spot size of about 100-400 µm; (ii) the free spectral range (FSR) should guarantee to observe two WGMs within the tuning range of the VCSEL used as light-source (Note: this choice limits slightly the maximum sensitivity reached, but assures the compatibility of the sensor with VCSEL and silicon detectors).

Microring resonators are easily integrated in planar optical circuits through evanescent coupling with a bus waveguide. With the aim of improving the design robustness and the fabrication tolerance, we adopted the directional coupler concept described above. To obtain the critical coupling condition with this scheme, a finite-length coupling zone should be designed, so that a resonator shape is transformed from a ring to a so-called *racetrack*.

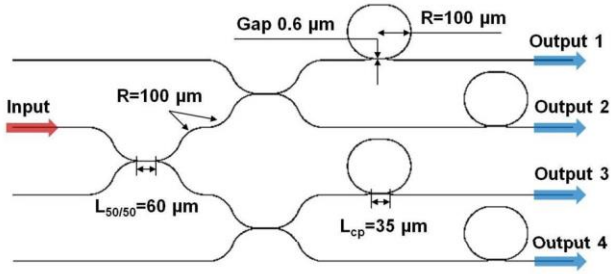

Fig. 3. CAD design of the optical circuit.

In fact, in the racetrack configuration the coupling occurs between two straight identical waveguides, so that the transfer matrix of waveguide-racetrack coupler can be associated with the matrix of directional coupler as follows [27]:

$$\sin(C \cdot L_{cr}) = k, \quad (2)$$

where C and k are coupling coefficients for the directional coupler and for the resonator-waveguide system, respectively; L_{cr} is the length which assures critical coupling to the resonator. C can be found as $C=\pi/4L_{50/50}$, while k depends on the loss coefficient of the resonator α_r as:

$$k^2 = 1 - \exp(-2\pi R \cdot \alpha_r) \quad (3)$$
$$\alpha_r = (2\pi n_g)/(Q_{\text{int}}\lambda),$$

where R is the radius of the bent part of the resonator, n_g is the group index and Q_{int} is the intrinsic quality factor of a resonator, twice larger than the one measured in critical coupling regime (Q_{meas}). Quality factors of about 6×10^4 at critical coupling conditions have been achieved in our laboratory for similar resonator systems [22]. Considering this prior knowledge, we assumed in the calculations Q_{meas} as high as 5×10^4. Using the equations (2) and (3) and the data of Table I, we obtained critical coupling length of 22 µm and 35 µm for resonator with R=100 µm covered with TEOS and with water, respectively.

Lastly, we performed eigenfrequency analysis with FEM solver to calculate the WGMs supported in the ring of radius 100 µm around desired wavelength (850 nm). For such a large resonator we obtained a FSR as small as 0.7 nm. Such spectral density of modes guarantees the presence of two resonances within the tuning range of 1.61 nm of our VCSEL (849.03 nm - 850.64 nm).

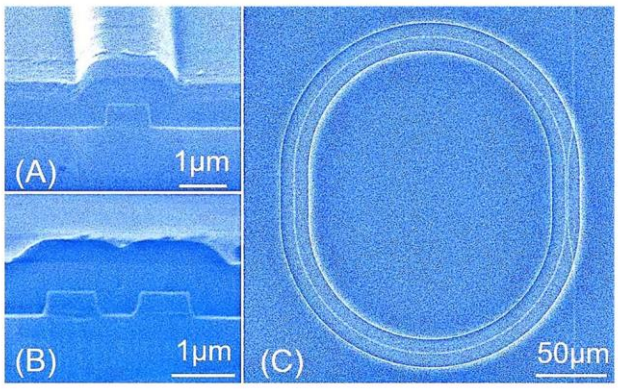

Fig. 4. Cross-sectional SEM images of the channel waveguide (A) and of the directional coupler (B). Top-view SEM image of the sensor ring with a window opened in the cladding (C).

Finally, based on the performed simulations, we designed an optical circuit optimized for multiplexed biosensing experiments. The layout of the circuit is sketched in Fig. 3. The device comprises an array of microring resonators with 35 µm-long coupling zone and 600 nm-wide separation with the bus waveguides. The radius of curvature of 100 µm was chosen on the base of the calculations of radiation losses in the curved waveguides. The resonators are ordered chequerwise in order to optimize and to simplify chemical functionalization of the sensors. Directional couplers are used to split the ligth into the four resonators. According to the simulations, the 3-dB coupling length was set to the value of 60 µm. The chosen length is robust towards small fabrication defects.

III. Fabrication

The devices were fabricated on commercial silicon wafers with a 4 µm-layer of thermal silicon oxide, thick enough to prevent the leakage of guided mode towards the substrate. High quality SiON films were deposited by PECVD. The mixture of gases (NH_3, N_2O, and SiH_4 diluted in N_2), introduced in the reaction chamber, and deposition parameters define the bulk refractive index and the composition of SiON film. The refractive index was adjusted to 1.66 by tuning the flow rate ratio $NH_3/(SiH_4+NH_3+N_2O)$ to 23%. The plasma power of 150 W and platen temperature of 300^{0}C were applied for the deposition. We deposited layers of different thicknesses, BS1 (320 nm), BS2 (350 nm) and BS3 (400 nm), in order to compensate possible film shrinkage of various degree during the thermal treatment. The structures were defined by standard UV-lithography and reactive-ion etching (RIE). With respect to our earlier work, we improved these fabrication steps in order to obtain geometries (principally - the waveguide width) closer to the simulated ones. The process was followed by a high temperature annealing step at 1050^{0}C for 1.5 hour to reduce the content of OH- and NH- groups in SiON, which contribute to propagation losses.

SiON films, especially after thermal annealing, have a very large tensile stress, similar to the one of silicon nitride

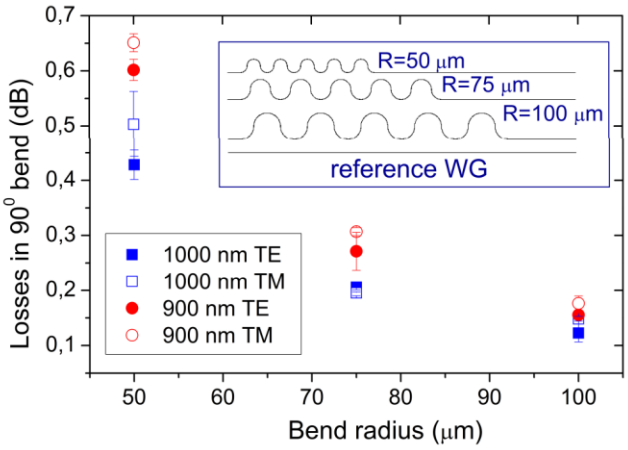

Fig. 5. Bending losses as a function of radius of curvature for waveguides with nominal widths of 900 nm and 1000 nm (BS3 sample). Inset: schematic of the test structures.

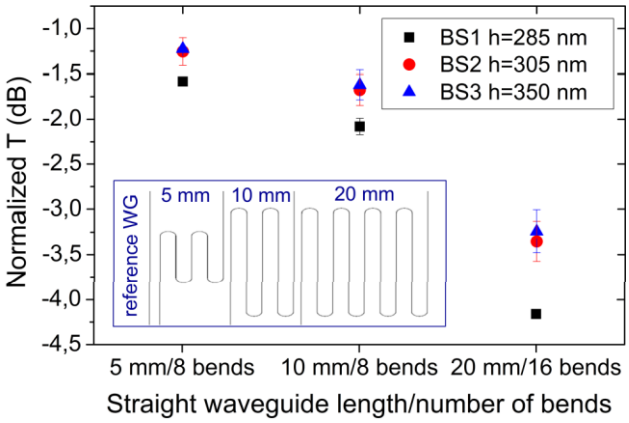

Fig. 6. Normalized transmittance (T) of the fabricated waveguides (nominal W=1000 nm) of different height (h) and length, measured in TE polarization. Error bars take into account measurements on several chips. Inset: schematic of the test structures.

grown via low-pressure chemical vapor deposition (LPCVD), which can easily lead to fractured film. To reduce the risk of cracking, we defined the optical structures by reactive-ion etching before the thermal annealing. In this way the area of the wafer covered with highly stressed material is drastically reduced, leading to the relaxation of the residual stress. In fact, the inspection of the final structures, performed with both optical and electron microscopy, did not give any evidence for stress-induced fractures. It should be noted that thermal treatment leads to a feasible decrease of film thickness (around 8-15%), common for PECVD-deposited films, and can also result in a slight change of the material refractive index due to the reduction of microvoids formed during the deposition.

The annealed samples were then covered with 1µm of TEOS oxide deposited by LPCVD to obtain the top cladding. In order to define the sensor site, a 20 µm-wide window was patterned above the ring by using photolithography (see also the SEM image of the sensor window in Fig.4(C)). The TEOS cladding was removed in these windows by dry RIE followed by wet etching in buffered HF solution. This two-steps procedure helps to uncover the sensor rings without waveguide perturbation. Finally, the wafers were diced in chips along the lines, preliminary defined by deep reactive-ion etching (DRIE). Such trenches prevent direct contact of the waveguide facets with the dicer allowing for much higher quality of the facets and, consequently, lower insertion losses.

Scanning electron microscopy and ellipsometry were used during and after the fabrication to perform an accurate control of geometries and refractive indices, and to allow for better comparison between optical design and measurement results. The refractive index of the annealed SiON waveguide was found to be 1.66±0.003 and is unchanged with respect to the as-deposited film, within the accuracy of the measurements. Cross-sectional SEM images of the isolated and coupled waveguides are shown in Fig. 4(A), (B). The fabricated channel waveguides are nearly rectangular. With respect to the nominal dimensions in our design, we measured a reduction of the width of ~6%. The SEM and ellipsometry analyses indicate a thickness shrinkage of ~10-12% relative to

the as-deposited SiON. Therefore the actual core heights become 285 nm, 305 nm and 350 nm for BS1, BS2 and BS3 samples, respectively. In the coupling zone of the directional coupler the situation changes. The vicinity of the waveguides on the reticule causes slight variations in exposure doses inducing different resist geometries, which are then transferred to the underlying SiON layer. One notes the presence of residual SiON on the extremes of both the waveguides, extending for about 80 nm into the gap between them. The waveguides are slightly trapezoidal in shape and are considerably narrower in comparison to the design (the width in the waveguide top is ~16% smaller than the nominal value).

IV. Optical Characterization

For optical characterization of the samples we used a standard setup for waveguide probing. As a light source, we used a single-mode VCSEL ULM850-B2-PL from *Philips Technologie GmbH U-L-M Photonics*, connected to a single mode fiber. The VCSEL can be tuned in wavelength around 850 nm by changing the driving current. A wave function generator is thus used to sweep continuously its output. Polarization state is defined with a rotating wave plates (retarders), mounted between two couplers/collimators. A fraction of the light from the VCSEL is probed as a reference signal. The rest of the power is launched into the input waveguide of the optical chip through a tapered fiber. Finally, a fiber-coupled silicon PIN photodetector and an oscilloscope are used to collect the output signals.

A. *Bending losses*

We characterized waveguides with multiple bends of different radius of curvature (Fig. 5, inset), comparing the measured output optical powers with that of the reference one, which is a perfectly straight 3 mm-long waveguide.

As an example, we show in Fig. 5 the results of the measurements on sample BS3. The same trend of exponential increas of bending losses with decrease of the radius was observed for all the samples. As expected, the losses for waveguides with W=1000 nm in TE polarization are the lowest, while the 900 nm-wide waveguides in TM polarization demonstrate the highest loss values. This difference, however, becomes relevant only for smaller radii, where the optical mode field undergoes stronger distortion passing the curves. Regarding the curve with radius of 100 µm, the lowest values of bending losses of 0.13 dB/90^0, 0.12 dB/90^0 and 0.12 dB/90^0 were found for W=1000 nm and TE polarization for BS1, BS2 and BS3 samples respectively. The difference between experimental data and the simulated values is attributed to: (i) the losses due to the surface roughness, omitted in the simulations; (ii) the mode mismatch effect which occurs at every junction of the straight and the bent waveguide, and is amplified due to the continuous change of the direction of light propagation in the bends of our test structures.

B. *Propagation losses*

The test structures for the evaluation of the propagation losses consisted of serpentine-like waveguides, with varying number of bends with curve radius of 100µm and varying distance between them (see Fig. 6, inset). This technique allows placing waveguides of different lengths on the very same chip. We measured optical power at the waveguide outputs for the same input optical power and, using a simple mathematical algorithm, calculated simultaneously the propagation losses of the straight waveguide and the bending losses in the curve.

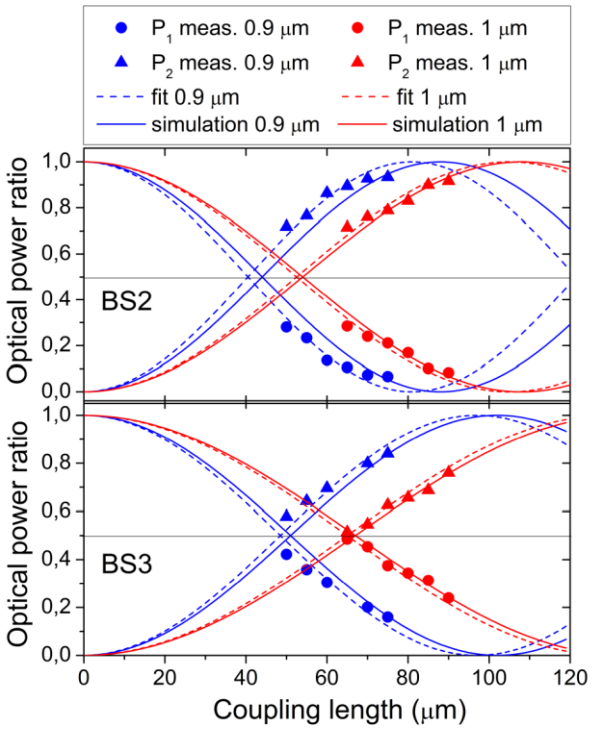

Fig. 7. Measured and re-calculated directional coupler splitting ratio as a function of coupling length and waveguide width (TE polarization).

Fig. 6 shows the normalized transmittance for the seprentine structures of samples BS1, BS2 and BS3, while all the values of propagation and bending losses, extracted from this experiment, are summarized in Table II. As predicted, the propagation losses decrease for larger waveguide dimensions, and are lower for stronger confined TE polarizied optical modes. In fact, the lowest loss coefficient of 0.79 dB/cm was

TABLE II
PROPAGATION AND BENDING LOSSES

Waveguide width	900 nm		1000 nm	
Polarization	TE	TM	TE	TM
Propagation losses (dB/cm)[a]				
BS1	1.11	1.36	1.00	1.05
BS2	1.01	1.10	0.84	0.94
BS3	0.88	0.95	0.79	0.81
Losses in 90^0 bend with radius of 100 µm (dB)[b]				
BS1	0.18	0.19	0.14	0.15
BS2	0.19	0.20	0.10	0.14
BS3	0.14	0.12	0.10	0.13

[a]The measurement errors are below 0.33dB/cm. [b]The measurement errors are below 0.08dB.

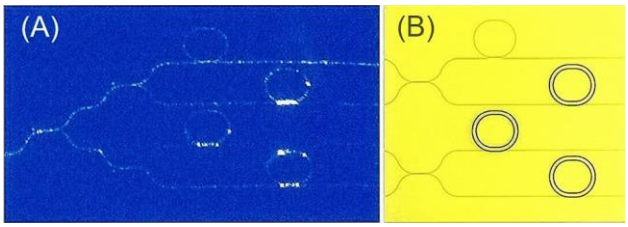

Fig. 8. Optical circuit illuminated with VCSEL (A) and microscopic image demonstating the sensing windows for water exposure (B).

found for 1000 nm-wide waveguide with the largest core thickness (sample BS3). However, no significant difference in propagation losses for W=900 nm and W=1000 nm has been observed, therefore both widths may be suitable for the circuit design. The values of propagation losses in our waveguides are comparable with recent reports on SiON waveguides operating at SW-NIR: in [28] the losses of 0.3 dB/cm were demonstrated for a waveguide with a core *n* of 1.515 and a cross-section of 1.1 μm × 2.2 μm. The values of bending losses in the 100 μm-curve obtained in this experiment confirm the measurements on multiply bent structures, presented in the previous section.

C. Directional coupler analysis

The analysis of the directional couplers was performed on two samples, BS2 and BS3, which are the ones with lower propagation and bending losses. We characterized the splitters with different coupling lengths for both waveguide widths in TE polarization. The measurement procedure was simple: launching the light in one of the splitter arm, we measured the optical power at both output branches, P_{out1} and P_{out2}, and the calculated corresponding optical power ratios as $P_i=P_{outi}/(P_{out1}+P_{out2})$, where i=1,2 indicates the output. The results of the measurements are reported in Fig.7. Regarding BS2 sample, we notice overcoupling of the splitters at all the available coupling lengths. Nevertheless, we could predict the correct $L_{50/50}$, fitting the data with the squared-sine function

$$P(z) = P_{in} \sin^2\left(\frac{\pi}{2L_{cp}} z\right), \quad (4)$$

that defines the power exchange between two parallel waveguides with negligible absorption losses. Here P_{in} is the input power, z is the distance in the direction of propagation, $L_{cp} = 2L_{50/50}$ is the coupling length for complete power transfer. Additionally, based on the SEM analysis, we re-calculated the 3-dB coupling length for the real geometry of the fabricated splitters, considering the trapezoidal shape, and, by using (4), calculated the theoretical power transfer. As it can be seen from Fig. 7, the agreement between the calculations and experimental results is very good and confirms the reliability of the theoretical method we used for design of our directional couplers.

For BS2, the actual values of coupling length $L_{50/50}$, derived from the fitted graph, are ~18-20% smaller with respect to the values in the initial design. As it was explained above, such alteration is caused by the deviation between simulated and obtained waveguide geometry. On the other hand, for BS3 samples the extracted 3-dB coupling lengths of 48 μm for W=900 nm and 65 μm for W=1000 nm match precisely with the initial design simulations. In this case, the waveguide thickness of 350 nm, larger than specified in design, compensates the decrease of the width, recovering the confinement factor and leading to an almost perfect 50/50 power splitting. Since in the design of the sensor circuit the coupling distance was set to 60 μm, we then expect to observe well-balanced light splitting for BS3 samples.

D. WGM resonance spectra

Finally, we performed an analysis of the optical circuit for samples BS2 and BS3. Fig. 8 (A) demonstrates light propagation in the circuit illuminated with VCSEL. The TE-polarized light from the input waveguide splits through the slightly overcoupled directional couplers and couples into four resonators. The characterization of the resonators in water was performed under continuous flow of aqueous solution over three opened sensor rings (shown also in Fig. 8 (B)), through the use of a homemade PDMS microfluidic flow cell.

The measured transmission spectra for the resonators covered with TEOS are presented in Fig. 9, while the spectra of the rings exposed to water are shown in Fig. 10. A fit of the normalized intensity was made using a Lorentzian function, summed with a sinusoidal function that accounts also for the effect of the Fabry–Pérot interference [29]. In both cases we observed clear resonances at wavelengths around 850 nm. The experimantal values of the FSR of about 0.67 nm-0.70 nm are in excellent agreement with that obtained in our design study of WGMs. Quality factors of 4.3×10^4 and 4.6×10^4 were found for the TEOS-covered resonators of BS2 and BS3 samples, respectively. The corresponding extracted intrinsic quality factors are one order of magnitude higher (4.5×10^5 and 3.8×10^5). To understand if the resonators are either in the undercoupling or in the overcoupling regime, we characterized several rings with the radius of curvature of 100 μm and different coupling lengths. From the results shown in

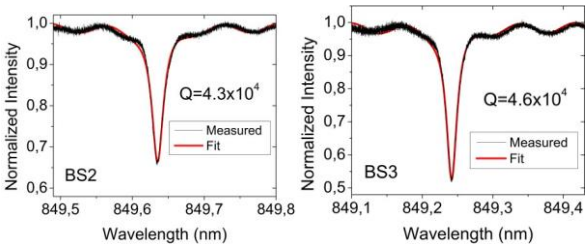

Fig. 9. Normalized waveguide transmission spectra of the microring resonators covered with silica (TE polarization).

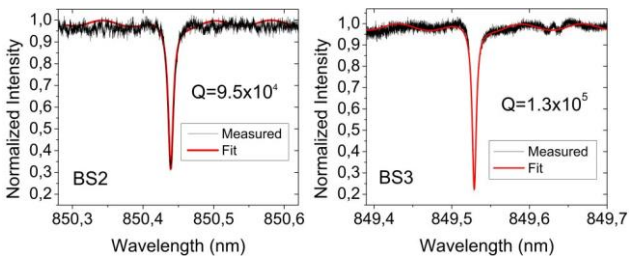

Fig. 10. Normalized waveguide transmission spectra of the microring resonators in water (TE polarization).

Fig. 11 we note that critical coupling for the fabricated resonators is achieved for the coupling length of around 10-20 µm. It is also evident that the resonators in the circuit (marked on the graph with the red labels) are in the overcoupling regime. This is caused partially by the deviation between designed and final geometry of the waveguides, but mostly by excessively long coupling zone. This is reasonable, since the resonators were designed for operation in acquous system, while the covered rings are rather used to get a first insight of the circuit performances.

We estimated the propagation losses inside the covered ring per unit length using the following expression [29]:

$$\alpha_r = \lambda_{res} / (Q_{\text{int}} \cdot FSR(\lambda_{res}) \cdot R), \quad (5)$$

where λ_{res} is the resonant wavelength, Q_{int} is the intrinsic quality factor, *FSR* is the free-spectral range, and *R* is the radius of the resonator. For BS3 sample, we calculated α_r as high as 1.5 dB/cm (0.35 cm^{-1}). With such a coefficient, the losses in the ring with circumference of 700 µm are estimated to be of the order of 0.1 dB. On the other hand, the ring resonator represents a closed waveguide with 100 µm-radius of curvature. Considering the bending losses from Table II, we obtained the losses in the resonator as high as 0.4 dB. This discrepancy validates that the mode mismatch effect in the racetrack is actually moderate and is less relevant with respect to the test curved structures.

Additionally, we calculated actual critical coupling lengths L_{cr}, using the algorithm explained in the section II, where we apply extracted coupling coefficients *C* and *k*. In this way, we obtained the lengths of 7 µm and 12 µm for TEOS-covered resonators of BS2 and BS3 sample, respectively.

Regarding the experiments on microrings in water, for sample BS2 we obtained critial coupling length of 10 µm, which differs significantly from the one set in the design (35 µm). Overcoupling in these resonators resulted in reduced *Q* factors (9.5×10^4) and considerably low values of extinction ratio (ER) of 5 dB. Nevertheless, such peak resolution of the optical transducer potentialy allows for successful sensing experiments with analytes in water. High sensitivity sensors, based on microring resonators, have been demonstrated for similar *Q* [1]. The resonators of BS3 sample measured in water demonstrated even higher quality factors of about 1.3×10^5 and ER of 6.5 dB. In fact, for these resonators the extracted value of L_{cr} in water (24 µm) is closer to the coupling zone fixed in the design.

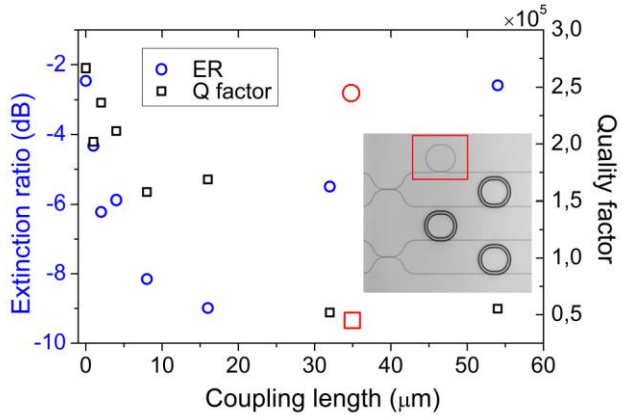

Fig. 11. Extinction ratio and quality factor analysis for the resonators with different coupling length. Red labels indicate the measured parameters of the TEOS-covered ring in the circuit of BS3 sample (shown also in the inset).

V. Volumetric Sensing

Sensitivity - In the end, we characterized the performance of our sensors by measuring the bulk sensitivity (*S*) of the opened resonators. This parameter is defined as the ratio of a spectral shift of the WGM resonances to a change of the bulk refractive index of solution flowing on top of the microring. For this experiment, the sensors were exposed to glucose-water solutions of various concentrations. The refractive index of such solutions can be easily estimated [30]. The resonance shift was measured simultaneously on three sensors of the same circuit. As an example, in Fig. 12 we show the results of the measurements on BS2 sample. We note, that the resonance shift was set to zero when as a reference liquid MES buffer was continuously flown over the sensor surface.

We observed that all the three sensors on the same sample have very similar sensitivities. For BS2 the sensitivity was found to be ~80 nm/RIU, with the difference between each resonator lower than 1%. For BS3 rings we observed slightly lower sensitivivy of ~68 nm/RIU. This is resonable, since WGMs of these resonators are more confined, and their interaction with the sensing solution is reduced.

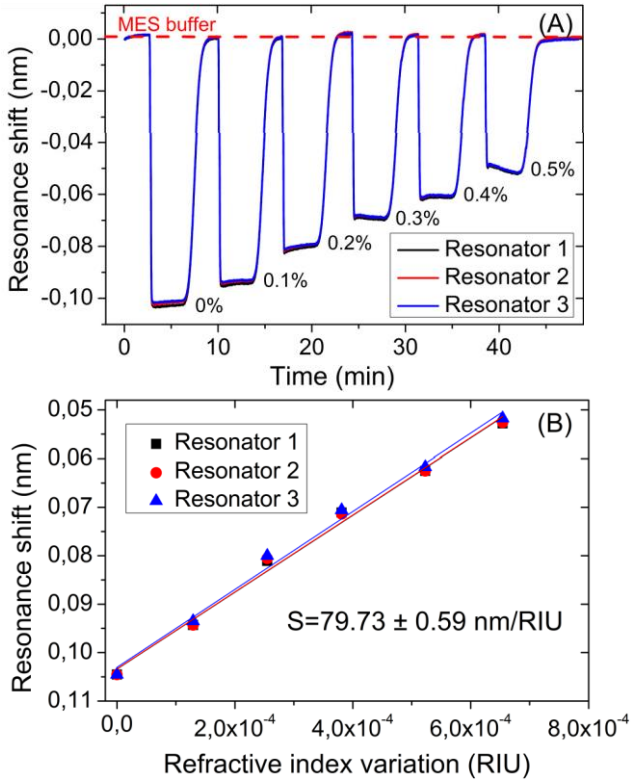

Fig. 12. Bulk sensitivity measurements on three opened microring resonators of BS2 sample for TE polarization. (A) The temporal evolutions of the resonance wavelength upon subsequent injections of water-glucose solutions at different concentrations . (B) Corresponding resonance wavelength shifts as a function of refractive index variation.

Limit of Detection – We calculated the corresponding limit of detection (LOD) of the sensors, defined as the minimum input quantity that can be distinguished with more than 99% fidelity. This parameter can be calculated as $LOD=3\in/S$, where $\in$ is the output uncertainty, given as the standard deviation obtained on repeated measurements of blank solution (where no analyte is present). From the measurement on three microring resonators, we observed always the same value of LOD of ~3×10^{-6} RIU for BS2 sample. The very similar values of bulk sensitivity and LOD for all the three microring resonators indicate the possibility of using our devices for multianalyte sensing.

On the optimum sample we performed surface sensing measurements [21, 23]. After surface functionalization with DNA-aptamers we flowed a solution where in a DMSO buffer Aflatoxin M1 toxin was diluted. The lowest concentration of Aflatoxin M1 that we were able to detect was 1.58 nM [23].

VI. Conclusions

In this paper we demonstrated design, realization and characterization of an optical circuit based on SiON waveguides. The circuit was designed for a lab-on-chip label-free sensor system using a low-cost VCSEL with emission at ~850 nm as light source. The microring resonators were optimized for sensing of analytes in aqueous systems.

We developed a series of test structures for characterization of specific circuit components, investigating fundamental performance parameters, such as propagation losses, bending losses, directional couplers splitting ratios and quality factors of resonators.

Propagation losses as low as 0.8 dB/cm were obtained for 350 nm × 950 nm waveguides in TE polarization. For the same waveguide geometry bending losses in the curve with radius of 100 µm were found to be 0.1 dB/90^0. Directional couplers based on such waveguides demonstrated 49/51 splitting ratio for 65 µm-long coupling zone. Finally, we achieved high quality factors up to 1.3×10^5 for the resonators immersed in water.

Bulk sensitivity of the sensors was evaluated. A sensitivity of 80 nm/RIU and LOD as low as 3×10^{-6} RIU were found, which is equivalent to 2.18×10^{-3} gr/100ml of glucose concentration, and the three sensors located on the same chip showed always the very same behavior. This proves that the technology can be used for multianalyte sensing.

This study demonstrates that SiON is a viable material platform for implementation of a high-performance and cost-effective photonic sensors.

Acknowledgment

This work was supported by the FP7 EU project "Symphony" (Grant agreement no: 610580). The authors gratefully acknowledge MNF Facility of Fondazione Bruno Kessler, Centre for Materials and Microsystems, for device fabrication. We also would like to thank Martino Bernard for helpful discussions.

References

[1] M. Estevez, M. Alvarez, L. Lechuga, "Integrated optical devices for lab-on-a-chip biosensing applications", Laser Photonics Reviews, vol. 6, no. 4, pp. 463-487, July 2012.

[2] J. Homola, "Surface Plasmon Resonance Sensors for Detection of Chemical and Biological Species" Chemical Reviews 2008 108 (2), 462-493.

[3] C. Ciminelli, C.M. Campanella, F. Dell'Olio, C.E. Campanella, M.N. Armenise, "Label-free optical resonant sensors for biochemical applications", Progress in Quantum Electronics, Volume 37, Issue 2, March 2013, Pages 51-107.

[4] Yuze Sun, Xudong Fan, "Optical ring resonators for biochemical and chemical sensing", Analytical and Bioanalytical Chemistry, vol. 399, no. 1, pp. 205-211, January 2011.

[5] Chao C-Y and Guo L J 2003 Biochemical sensors based on polymer microrings with sharp asymmetrical resonance Appl. Phys. Lett. 83, no. 8, pp. 1527–1529, August 2003.

[6] R. C. Bailey , A. L. Washburn , A. J. Qavi, M. Iqbal, M. Gleeson, F. Tybor, L. C. Gunn, "A robust silicon photonic platform for multiparameter biological analysis". Proc. SPIE 7220, Silicon Photonics IV, 72200N, February 2009.

[7] F. Vollmer, L. Yang, "Label-free detection with high-Q microcavities: A review of biosensing mechanisms for integrated devices", Nanophotonics 2012, 1, 267–291.

[8] W. Bogaerts, P. de Heyn, T. van Vaerenbergh, K. de Vos, S. Kumar Selvaraja, T. Claes, P. Dumon, P. Bienstman, D. van Tourhout, R. Baets, "Silicon microring resonators". Laser Photonics Rev. 2012, 6, 47–73.

[9] K. De Vos, I. Bartolozzi, E. Schacht, P. Bienstman, and R. Baets, "Silicon-on-Insulator microring resonator for sensitive and label-free biosensing," Opt. Express, vol. 15, no. 12, pp. 7610-7615, May 2007.

[10] S.T. Fard, V. Donzella, S.A. Schmidt, J. Flueckiger, S.M. Grist, P. Talebi Fard, Y. Wu, R.J. Bojko, E. Kwok, N.A. Jaeger, D.M. Ratner , L. Chrostowski,. "Performance of ultra-thin SOI-based resonators for sensing applications". Opt Express. 2014 Jun 16;22(12):14166-79.

[11] C. Ciminelli, F. Dell'Olio, D. Conteduca, C.M. Campanella, M.N. Armenise, "High performance SOI microring resonator for biochemical sensing", Optics & Laser Technology, Volume 59, July 2014, Pages 60-67.

[12] Iqbal, M.A. Gleeson, B. Spaugh, F. Tybor, W.G. Gunn, M. Hochberg, T. Baehr-Jones, R.C. Bailey, L.C. Gunn, "Label-free biosensor arrays based on silicon ring resonators and high-speed optical scanning instrumentation", IEEE J. Sel. Top. Quantum Electron. Vol. 16, no. 3, pp. 654-661, May 2010.

[13] M. A. Cooper, *Label-Free Biosensors: Techniques and Applications*, Cambridge University Press, New York, 2009.

[14] G.M. Hale, M.R. Querry, "Optical constants of water in the 200 nm to 200 µm wavelength range", Appl. Opt. 12,no. 3, pp. 555-563, 1973.

[15] R. Heideman, M. Hoekman, E. Schreuder, "TriPleX-Based Integrated Optical Ring Resonators for Lab-on-a-Chip and Environmental Detection," Selected Topics in Quantum Electronics, IEEE Journal of , vol.18, no.5, pp.1583-1596, September-October 2012.

[16] A. Samusenko, G. Pucker, D. Gandolfi, R. Guider, M. Ghulinyan, F. Ficorella, L. Pavesi, "Integrated silicon photodetector for lab-on-chip sensor platforms", Proceedings of SPIE, vol. 9520, 95200D, June 2015.

[17] M. Weisser, G. Tovar, S. Mittler-Neher, W. Knoll, F. Brosinger, H. Freimuth, M. Lacher, W. Ehrfeld, "Specific bio-recognition reactions observed with an integrated Mach–Zehnder interferometer", Biosensors and Bioelectronics, vol. 14, no. 4, pp. 405-411, April 1999.

[18] Sung Joong Choo, Jinsik Kim, Kyung Woon Lee, Dong Ho Lee, Hyun-Joon Shin, Jung Ho Park, "An integrated Mach–Zehnder interferometric biosensor with a silicon oxynitride waveguide by plasma-enhanced chemical vapor deposition", Current Applied Physics, vol.14, no. 7, pp. 954-959, July 2014.

[19] G. H. Cross, A. Reeves, S. Brand, M.J. Swann, L.L. Peel, N.J. Freeman, J.R. Lu, "The metrics of surface adsorbed smallmolecules on the Young's fringe dual-slabwaveguide interferometer", Journal of Physics D: Applied Physics, vol. 37, no. 74, pp. 74-80, April 2004.

[20] K. Mogensen, P. Friis, J. Hübner, N. Petersen, A. Jørgensen, P. Telleman, and J. Kutter, "Ultraviolet transparent silicon oxynitride

waveguides for biochemical microsystems," Optics Letters, vol. 26, no. 10, pp. 716-718, May 2001.

[21] R. Guider, D. Gandolfi, T. Chalyan, L. Pasquardini, A. Samusenko, C. Pederzolli, G. Pucker, L. Pavesi, "Sensitivity and Limit of Detection of biosensors based on ring resonators", Sensing and Bio-Sensing Research, to be published. Available online August 2015.

[22] R. Guider, D. Gandolfi, T. Chalyan, L. Pasquardini, A. Samusenko, G. Pucker, C. Pederzolli, L. Pavesi "Design and optimization of SiON ring res-onators-based biosensors for Aflatoxin M1 detection", Sensors, vol. 15, no. 7, pp.17300-17312, July 2015.

[23] T. Chalyan, D. Gandolfi, R. Guider, L. Pasquardini, A. Samusenko, C. Pederzolli, G. Pucker, L. Pavesi, "Characterization of SION microring resonators for biosensing applications", Biophotonics, 2015 International Conference, IEEE Xplore, 1-4, November 2015.

[24] D. Gandolfi, F. Ramiro-Manzano, F. J. Aparicio Rebollo, M. Ghulinyan, G. Pucker, L. Pavesi, "Role of Edge Inclination in an Optical Microdisk Resonator for Label-Free Sensing", Sensors, vol. 15, no. 3, pp. 4796-4809, February 2015.

[25] D.G. Rabus, *Integrated Ring Resonators*, Springer Berlin-Heidelberg, 2007.

[26] Q. Wang, G. Farrell, T Freir, "Effective index method for planar lightwave circuits containing directional couplers", Optics Communications, vol. 259, no. 1, pp.133-136, March 2006.

[27] M. Soltani, S. Yegnanarayanan, Li Qing, A. Adibi, "Systematic Engineering of Waveguide-Resonator Coupling for Silicon Microring/Microdisk/Racetrack Resonators: Theory and Experiment", Quantum Electronics, IEEE Journal of , vol.46, no.8, pp.1158-1169, August 2010.

[28] T.Tsuchizawa, T. Watanabe, K. Yamada, H. Fukuda, S. Itabashi, J. Fujikata, A. Gomyo, J. Ushida, D. Okamoto, K. Nishi, K. Ohashi, "Low-loss Silicon Oxynitride Waveguides and Branches for the 850-nm-Wavelength Region", Japanese Journal of Applied Physics, vol. 47, no. 8S1, pp. 6739, April 2008.

[29] L. Stefan, M. Bernard, R. Guider, G. Pucker, L. Pavesi, M. Ghulinyan, "Ultra-high-Q thin-silicon nitride strip-loaded ring resonators," Opt. Lett. 40, no. 14, pp. 3316-3319, July 2015.

[30] W. M. B. M. Yunus, A. B. A. Rahman, "Refractive index of solutions at high concentrations," Applied optics, vol. 27, no. 16, pp. 3341-3343, August 1988.